Earth's albedo and its symmetry

George Datseris[1], **Bjorn Stevens**[1]

[1]Max Planck Institute for Meteorology, Hamburg, Germany

Key Points:

- Surrogate time-series analysis establishes the hemispheric albedo symmetry but fails to identify mechanisms enforcing this symmetry.
- Decadal trends in reflected insolation, while substantial, fail to break Earth's hemispheric albedo symmetry.
- Hemispheric clear-sky albedo asymmetries are balanced by hemispheric asymmetries in storm-track cloudiness.

Corresponding author: George Datseris, `george.datseris@mpimet.mpg.de`

Abstract

The properties of Earth's albedo and its symmetries are analyzed using twenty years of space-based Energy Balanced And Filled product of Clouds and the Earth's Radiant Energy System measurements. Despite surface asymmetries, top of the atmosphere temporally & hemispherically averaged albedo appears symmetric over Northern/Southern hemispheres. This is confirmed with the use of surrogate time-series, which fails to refute the hypothesis that the hemispheric albedo difference is distinguishable from zero. An analysis of reflected irradiance time-series fails to find any indicators of some dynamics enforcing this albedo symmetry. This analysis shows that variability in the reflected solar irradiance is almost entirely (99 %) due to the seasonal (yearly and half yearly cycle) variations, mostly due to seasonal variations in insolation. Hemispheric residuals of the de-seasonalized reflected solar irradiance are not only small, but indistinguishable from noise, and thus not correlated across hemispheres. The residuals contain a global trend that is large, as compared to expected albedo feedbacks, and is also hemispherically symmetric. Neither the magnitude of these trends nor its symmetry – which could be indicative of a symmetry preserving cloud dynamics – is well understood. To pinpoint precisely which parts of the Earth system establish the hemispheric symmetry, we create an energetically consistent cloud-albedo field from the data. We show that the surface albedo asymmetry is compensated by asymmetries between clouds over extra-tropical oceans, with southern hemispheric storm-tracks being 11% cloudier than their northern hemisphere counterparts.

Plain Language Summary

The planetary albedo is the portion of solar radiation reflected by the planet back to space, and is a prime factor deciding whether the planet will warm or cool over time. An intriguing property of the albedo is that, on average, Northern or Southern Hemisphere (NH or SH) have the same albedo, called hemispheric symmetry. The symmetry is surprising, because SH has much more ocean than land, and ocean is less reflective than land, so NH should have higher albedo. Nevertheless, clouds, which also tune the albedo, compensate the surface albedo imbalances of the two hemispheres, leading to an overall symmetric albedo. It is so far unclear how, or why, clouds perform this compensation. Here we show that this cloud compensation comes from the extra-tropical storm tracks of the SH, which are cloudier than those of the NH. We further analyze satellite radiation measurements in search of indicators of a process between NH and SH which establishes the albedo symmetry. While we find reflected radiation timeseries to be mostly a seasonal cycle superimposed with small noise, we also see that reflection decreases overtime with a significant trend that is identical for both hemispheres and thus hints at some interaction mechanism.

1 Introduction

The planetary albedo α, an intrinsic property of a planet, measures the fraction of incident radiant energy (or insolation) that it reflects back to space. Its complement, the co-albedo $(1-\alpha)$ thus determines what fraction of that insolation, I, remains to heat the planet. Several components of the planet and interactions among them go into deciding the value of α. For Earth, the atmosphere and clouds are major contributors to albedo (Ramanathan, 1987), as are its surface properties (the land fraction, ice cover (Budyko, 1969) and even the biosphere (Betts, 2000)). Whereas the contributions of the constituent parts of the albedo have been studied in great detail, little attention has been devoted to understanding the properties of the albedo as a whole, as seen from space, and as one might do for another planet.

Clouds and Earth's Radiant System (CERES) (Loeb et al., 2018; Kato et al., 2018) datasets provide precise measurements of Earth's radiant energy balance as seen from

space. From these measurements it is possible to deduce the magnitude of Earth's planetary albedo, $\alpha \approx 0.29$, which varies surprisingly little across years (Stevens & Schwartz, 2012). Remarkably, the measurements show that on long-time averages the two hemispheres have the same albedo, which we refer to as the *hemispheric albedo symmetry* (Stevens & Schwartz, 2012; Voigt et al., 2013, 2014; Stephens et al., 2015, 2016; Haywood et al., 2016; Bender et al., 2017). In the simplest approximation this arises from the asymmetric response of clouds to surface albedo asymmetries (Voigt et al., 2013). As pointed out by Stevens and Schwartz (2012) (see also the review by (Stephens et al., 2015)), these properties of Earth's albedo, while seemingly fundamental to an understanding of Earth's climate, lack even the outline of a theoretical explanation. Yet more remarkable is the scarcity of work that attempts an explanation.

Early theoretical studies of Earth's albedo mostly focused on surface contributions to the planetary albedo, specifically the ice-albedo feedback first postulated by Arrhenius (1896). Work on this question flourished in the early 1970s, see Budyko (1969); Sellers (1969); North (1975); Chýlek and Coakley (1975); Stone (1978) among others. These studies sought to understand how the surface albedo depends on, and in turn influences, the planetary temperature, but they did so by taking clouds for granted. In effect, they assumed that, despite being by far the dominant and most dynamic component of the planetary albedo (as later shown in pioneering work by Ramanathan (1987)), secular changes in cloudiness are negligible. The early work also assumed, albeit implicitly, hemispheric symmetry. Such an assumption seems natural, until one asks why clouds should vary between the hemispheres in a way that counterbalances a large, $6\,\mathrm{W\,m^{-2}}$, surface radiation asymmetry (see below), yet somehow be independent of a temporally changing climate state.

Our work is motivated by the intellectual tension that arises from the assumed constancy of clouds over long timescales on one hand, and the fact that they compensate the surface albedo asymmetry to result in overall symmetric albedo on the other hand. We build upon earlier observational studies by Donohoe and Battisti (2011); Loeb et al. (2019), who decomposed the TOA albedo value and time-anomalies into a surface and atmosphere contribution, and by Voigt et al. (2013), who showed that the hemispheric albedo symmetry is neither a trivial property of the Earth system, nor reproduced by comprehensive Earth system models. By using the new cloud-information provided in the latest release of CERES, we are able to create a new measure of cloudiness that allows us to better understand how, and to what extent, cloud variations influence albedo variations. Our analysis is further aided by more sophisticated methods of time-series analysis, and a near doubling of the length of the observational record as compared to what was available to Voigt et al. (2013). This allows a more rigorous quantification of properties of Earth's albedo that models or theories should explain, and provides context for observations from an increasing number of studies of the albedo of other planets (Cowan & Agol, 2011; Shields et al., 2013; Mansfield et al., 2019), some of which also identify a role for clouds (Kreidberg et al., 2014).

Our contributions are as follows. Using CERES data we show that the observed hemispheric albedo symmetry is a statistically indistinguishable from a perfect symmetry. This has been conjectured by previous studies, but not quantitatively demonstrated. We further analyse radiation time-series in search of indicators of dynamical communication mechanisms that establish the symmetry between the two hemispheres. The overwhelming majority of temporal variability is associated with the seasonal cycle. Residuals of the seasonal cycle are found to be indistinguishable from noise and as such provide no sign of an extra-seasonal component to the albedo dynamics. Nor do we find evidence in the radiation time-series record for an active process that maintains the hemispheric albedo asymmetry. However, a long-term trend in the albedo is shown to be hemispherically symmetric, which we would not expect in the absence such a process. We then construct a "cloudiness" field, representing physical cloud albedo, which is a better rep-

Table 1. Notation used in this paper.

Symbol	Description	Type
I	insolation	$\mathrm{W\,m^{-2}}$
R	all-sky refl. insolation at TOA	$\mathrm{W\,m^{-2}}$
K	clear-sky refl. insolation at TOA	$\mathrm{W\,m^{-2}}$
Y	Seasonal component of R	$\mathrm{W\,m^{-2}}$
α	all-sky albedo at TOA	fraction
α_K	clear-sky albedo at TOA	fraction
C	Cloud albedo	fraction
O	ice-free ocean area fraction	fraction
E	ice & snow/ice coverage	fraction
L	ice-free land fraction	fraction
$\mathcal{T}$	time average (proper)	operation
$\mathcal{N}$	northern hemisphere average	operation
$\mathcal{S}$	southern hemisphere average	operation
$\mathcal{G}$	global average, $\equiv (\mathcal{S}+\mathcal{N})/2$	operation
$\mathcal{Z}$	zonal average	operation
NH, SH	northern, southern hemisphere	abbrv.

resentation of clouds' impact on the shortwave part of the radiation balance than cloud fraction. Using this "cloudiness" we demonstrate that, as expected, the hemispheric albedo symmetry is a result of a hemispheric cloud asymmetry (see below). The cloudiness allows us to further demonstrate the extent to which average, versus spatiotemporal, cloud properties are responsible for observed cloud asymmetries. Unexpectedly we find that the major source of asymmetry is in the last place one would expect, over the ocean in the storm tracks, where the southern hemisphere is markedly more cloudy than the northern hemisphere, just enough so to exactly compensate the surface albedo asymmetry. In the conclusion section we discuss the potential impact of our work and the open questions that remain.

Terminology

Notation and symbols used in the text are summarized in Table 1. The reference to clear-sky adopts values defined by CERES and is estimated from scenes identified as being cloud free. "All-sky" denotes no sub-sampling of specific scenes. The $\approx$ symbol is used to indicate that a result has been rounded to the displayed digits, and the $\prime$ denotes a residual.

To account for the eccentricity of the Earth's orbit, as well as the uneven sampling of the orbit done by monthly averages, $\mathcal{T}$ weights every month by the number of days in that month. We additionally ensure that only full years (total time points multiple of 12) participate in the average. Not doing this can give wrong results. For example, $\mathcal{T}(\mathcal{N}(I)) - \mathcal{T}(\mathcal{S}(I)) \approx -0.002\ \mathrm{W\,m^{-2}}$, but using standard averaging of the first 240 months (20 full years currently available in CERES EBAF) instead of weighted gives $\approx -0.6\ \mathrm{W\,m^{-2}}$. Such large differences are reported in the literature, e.g. Fig. 4 of (Stephens et al., 2016), but are inconsistent with Kepler's second law, which has the direct result that each hemisphere receives the same amount of total insolation over a full orbital period.

By definition, $R = \alpha I$, with α the "albedo". For the energy balance we mostly care about the portion of insolation that is scattered back to space, which we will call *effective albedo* and define as R/I. It can only be estimated when $I \neq 0$. We use the

term *physical albedo* to distinguish the case when α is estimated in some other manner like surface or optical properties, and thus can be defined also for the case $I = 0$.

2 Properties of the reflected insolation, R

2.1 Albedo's value and hemispheric symmetry

The effective albedo is $\bar{\alpha} = \mathcal{G}(\mathcal{T}(R))/\mathcal{G}(\mathcal{T}(I)) \approx 0.291$. For clear-sky we have $\bar{\alpha}_K = \mathcal{G}(\mathcal{T}(K))/\mathcal{G}(\mathcal{T}(I)) \approx 0.156$. Clouds thus increase the planetary albedo (on average) by almost a factor of two. The hemispheric difference in R is, on average, $\mathcal{T}(\mathcal{N}(R)) - \mathcal{T}(\mathcal{S}(R)) \approx 0.1\ \mathrm{W\,m^{-2}}$, which is 0.1% of the global average ($\mathcal{T}(\mathcal{G}(R))$) and, as we will show, indistinguishable from 0. The same difference for the clear-sky is $\approx 6\ \mathrm{W\,m^{-2}}$, 11% of its global average.

We adopt two approaches to test the hypothesis that $\mathcal{T}(\mathcal{N}(R)) \neq \mathcal{T}(\mathcal{S}(R))$. For the first, we make use of surrogate time-series (Theiler et al., 1992; Lancaster et al., 2018) to approximate $\mathcal{N}(R)$ and $\mathcal{S}(R)$. To construct the surrogates we adopt the method of Small et al. (2001), which is adapted to periodic data. The surrogates are constructed from the data already contained in the signal, and are designed to have the same periodic structure as the signal, but phase information is scrambled, destroying any correlation between cycles. In essence the surrogates sub-sample the months with replacement (i.e. for all Aprils, some are repeated in the surrogates, some are shuffled around, while some others are skipped entirely). An example is shown in Fig. 1(a).

The hemispheric asymmetry of temporal averages of the surrogates, as estimated from several thousand surrogates of $\mathcal{N}(R)$ and $\mathcal{S}(R)$, gives a distribution of possible differences. In Fig. 1(c) we compare this with the real difference, and find that a vanishing (0) hemispheric asymmetry in the surrogate albedo is well within the 5-95% quantiles of the data, establishing that the observed value indistinguishable from zero.

For the second approach, we decompose hemispherically averaged R into a component Y containing the seasonal cycle and a residual $R'_{\mathcal{N}} = \mathcal{N}(R) - Y_{\mathcal{N}}$ for NH, similarly for SH, with the seasonal component defined as

$$Y(t) = A_0 + \sum_i A_i \cos(2\pi\omega_i t + \phi_i), \tag{1}$$

with ω_i the chosen frequencies of the decomposition. In our seasonal decomposition we include only the annual (12 month) and semi-annual (6 month) cycle, as both arise from the combination of Earth's obliquity and eccentricity. The fitting parameters, A_i, ϕ_i are estimated from the data, with A_0 the time mean, following Bagge Carlson et al. (2017), who transforms eq. (1) into a least squares problem in frequency space and works well even for non-equi-spaced time axis. Our approach differs from the time anomaly decomposition adopted by (Loeb et al., 2019) in that it makes the frequencies included in the "seasonal" variations explicit, thereby allowing us to write $Y(t)$ as an explicit function of the *physical* time t.

Through the decomposition (1), $A_{0,\mathcal{N}} = \mathcal{T}(\mathcal{N}(R))$, likewise for the southern hemisphere, hence $\mathcal{T}(R'_{\mathcal{N}}) = \mathcal{T}(R'_{\mathcal{S}})$ by construction. To quantify how likely it is to observe an asymmetry of $0.1\ \mathrm{W\,m^{-2}}$, simply due to the fact that our measured residuals have finite time length, we analyze $D = R'_{\mathcal{N}} - R'_{\mathcal{S}}$, where by definition $\mathcal{T}(D) = 0\ \mathrm{W\,m^{-2}}$. We model D as an auto-regressive process (Brockwell & Davis, 1996)

$$D_t = \sum_{i=1}^{M} \theta_i D_{t-i} + \eta_t \tag{2}$$

with η white noise (with same standard deviation as D), M the auto-regressive order and θ_i the parameter choices. Justification for this model is provided in §2.2. We estimate the parameters θ_i that best fit the measured time-series with the Levinson method

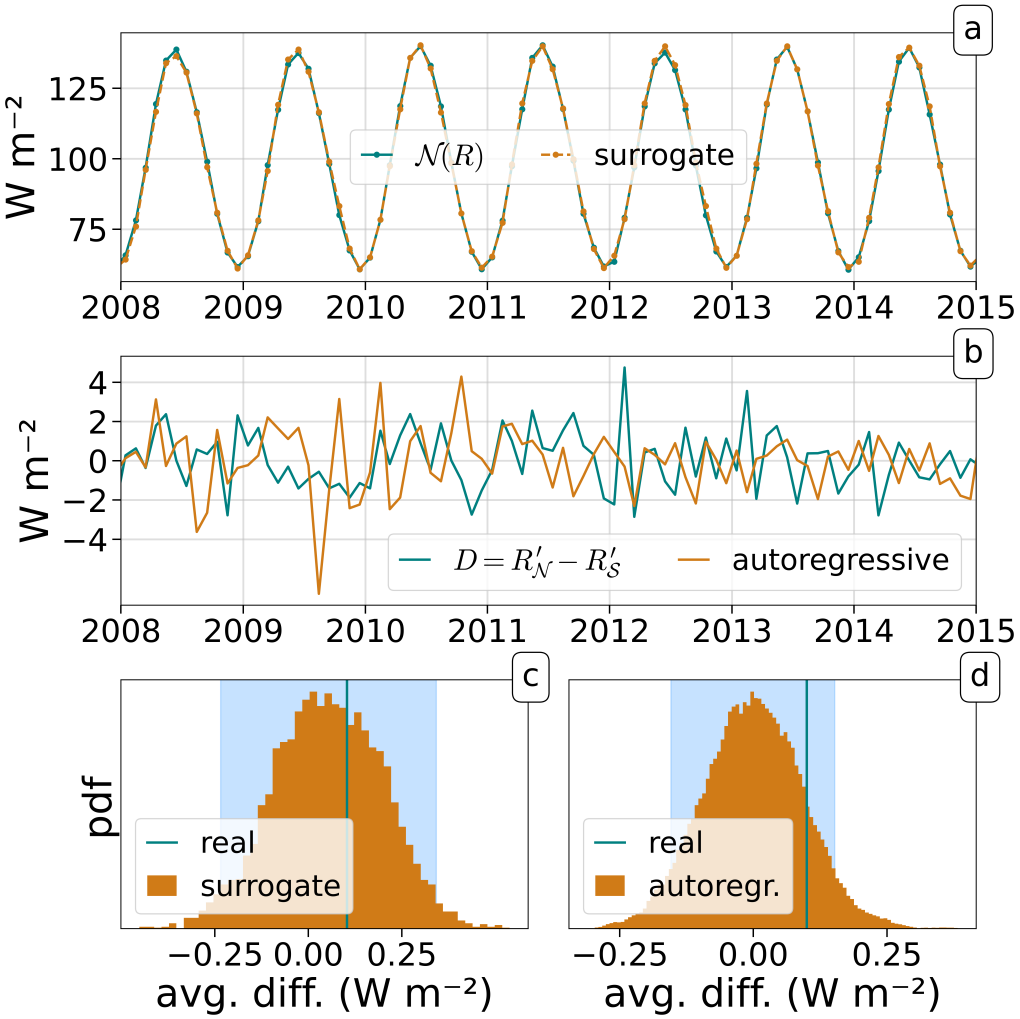

Figure 1. Hemispheric difference of R is indistinguishable from 0. (a) Hemispherically averaged R, $\mathcal{N}(R)$, and pseudoperiodic surrogate which follows same dynamics. (b) Difference of residuals of hemispherically averaged R time-series, and an autoregressive process with same correlation structure. (c) Possible values of time-averaged hemispheric difference for pseudoperiodic surrogates. (d) Like (c), but now possible values come from sub-sampling 20 years of an infinitely long autoregressive realization. Blue rectangles show the 5-95% quantiles.

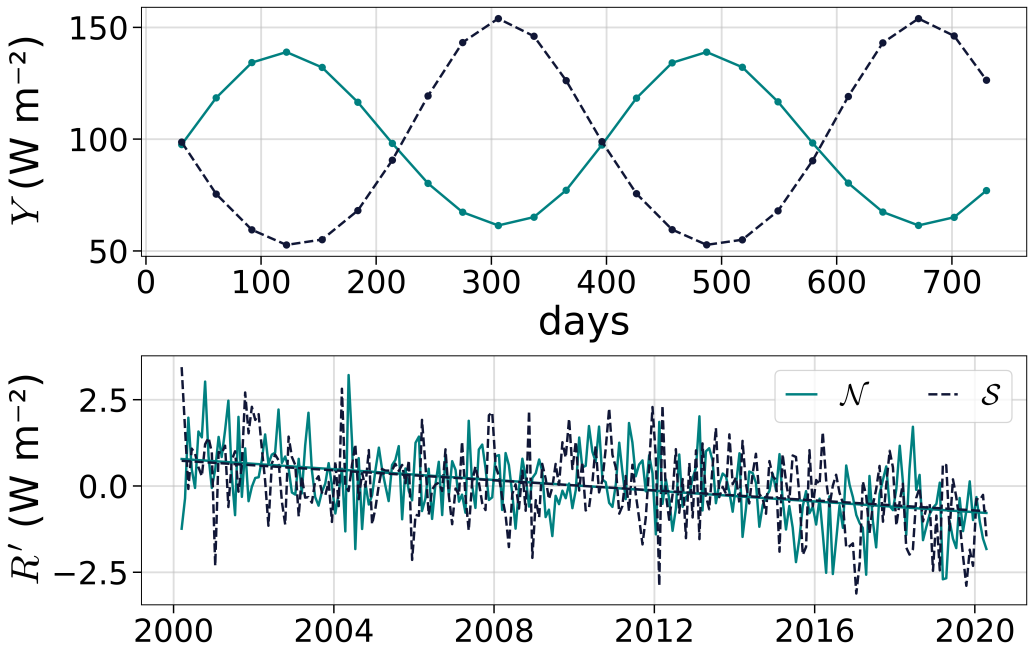

Figure 2. Seasonal decomposition of the reflected solar radiation R. The seasonal component s repeats identically for all time (and is plotted over days, because this time axis is used for the seasonal decomposition). Best line fit of the residuals is also plotted, and both hemispheres have a statistically significant trend of ≈ -0.006 W m^{-2}/month $= 0.7$ W m^{-2}/decade.

of linear predictive code (Levinson, 1946), using $M = 12$. Fig. 1(b) presents D and a realization of D_t. Using D_t we simulate a very long autoregressive time-series (that in the limit $t \to \infty$ has 0 mean by definition) and sample 242-long subsets of it and calculate their mean. The resulting distribution is shown in Fig. 1(d). It shows that measuring value 0.1 W m^{-2} simply because of finite time-span is a likely scenario.

The above analysis establishes the *hemispheric albedo symmetry*. This property of R was noted in the very first space-based measurements (Haar & Suomi, 1971), its systematic and quantitative study only became possible with the advent of the CERES data (Stevens & Schwartz, 2012; Voigt et al., 2013, 2014; Stephens et al., 2015, 2016; Haywood et al., 2016; Bender et al., 2017). Here we have shown that it is indistinguishable from zero. For the present value of 0.1 W m^{-2} to prove significantly different from 0 W m^{-2}, would require the distribution of Fig. 1d to have a standard deviation of $2\sigma \leq 0.1$ W m^{-2}. This, we calculate, would require at least fifty years of data. In the following subsections we analyze the radiation time-series further in search of an indication of dynamics, or communication, that leads to the hemispheric albedo symmetry.

2.2 Dynamics of residuals

If there were some process that established the hemispheric albedo symmetry, we might be able to identify it in the dynamics of $R'_{\mathcal{N}}$ and $R'_{\mathcal{S}}$. For instance if one hemisphere responded to internal anomalies that develop in the other hemisphere we would expect to see this in the correlation structure between the two time-series. Fig. 2, presents Y and R'. The ratio $\mathrm{Var}(Y)/\mathrm{Var}(R)$ is ≈ 0.99 for both NH and SH. With $\sigma_{R'} \approx 1.1$ W m^{-2} for either hemisphere, very little signal is carried by the hemispheric residuals. Also, apart

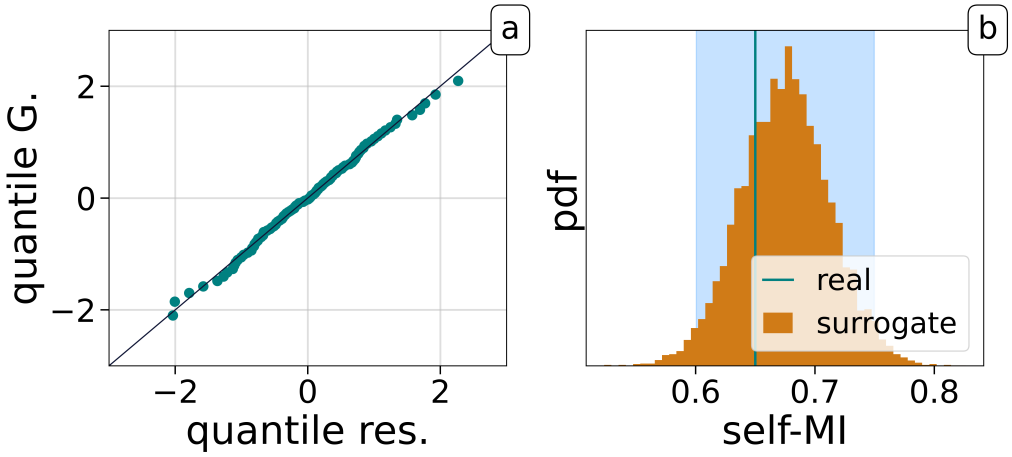

Figure 3. (a) A quantile-quantile plot of the quantile of the residuals versus the quantile of a Gaussian fitted to the residuals of NH. (b) Distribution of 1-step self-mutual-information of 10,000 truncated Fourier transform surrogates (see text), along with the value of the real time-series. Blue span shows the 5-95% quantiles of the distribution.

from a consistent downward trend in both hemispheres, no correlation exists between the time-series of R' in the two hemispheres. Nor, as detailed next, could we detect such relationships through a more quantitative analysis.

To test for the possibility of dynamics in the time series of R' we first try to reject the null hypothesis that it can be described by a linear Gaussian (stochastic) process. To do so we first compare the different quantiles of the data with those from a Gaussian distribution fit to the same data. The result falls almost exactly on the diagonal (Fig. 3(a)), which means that the original data can be modelled well from this distribution. Similarly, but not shown, a K-sample Anderson-Darling test (Scholz & Stephens, 1987) also fails to reject the null hypothesis. This establishes that the distribution of the data is Gaussian, but not whether their sequence is correlated, or just noise.

To explore this latter question we create a surrogate time-series for $R'_{\mathcal{N}}$ (we find identical results for SH, not shown) following the approach of Nakamura et al. (2006), which is designed to represent fluctuating data with constant trends. The surrogate follows a linear Gaussian process with autocorrelation the same as the input time-series, and same trend, and thus satisfies the null hypothesis by construction (the autocorrelation uniquely defines a linear Gaussian process (Brockwell & Davis, 1996)). We then attempt to distinguish this time-series from the actual time-series of $R'_{\mathcal{N}}$. To do so a 1-step self-mutual-information statistic is adopted as a discriminatory statistic q. This quantity is chosen as it has been shown to distinguish noise from determinism in small data sets (Lancaster et al., 2018). The distribution of values $p(q)$ can be constructed from different realizations of the surrogate. If the real data are significantly outside this distribution, the null hypothesis can be rejected. As Fig. 3(b) shows, the real q is well within the possible q of the null hypothesis (this is true for both NH and SH residuals), thus failing to reject the null hypothesis. The apparent lack of dynamics in the residuals of either hemisphere may simply be telling us that we have projected – through averaging – a too high dimensional dynamics onto a too low dimensional space (and thus the result is indistinguishable from noise due to extreme information loss). To test for this possibility we repeated the above analysis on $10^\circ \times 10^\circ$ longitude-latitude decompositions and reached similar conclusions. On yet smaller scales, Voigt et al. (2013) showed that albedo features become more strongly correlated with neighboring areas, and thus are

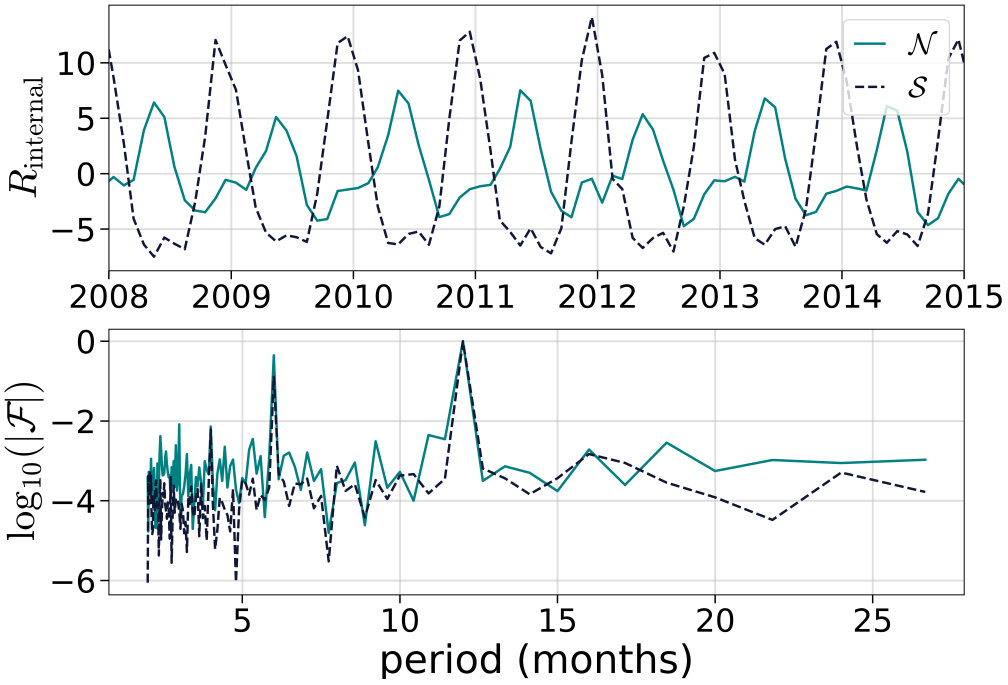

Figure 4. (a) Internal component of mean albedo decomposition of R. (b) Power spectrum of (a) (logarithm of absolute value of Fourier transform $\mathcal{F}$).

no longer independent samples. A principle component analysis also failed to identify dominant patterns of variability.

In summary, we were unable to identify any evidence of dynamics in the residual time-series. Based on a variety of tests we could find no basis for distinguishing extra-seasonal variations of R from noise. Given the strength of the trends in R' we find the lack of signal in R' surprising.

2.3 Temporal variability

The seasonal decomposition as applied in Eq. (1) removes seasonal fluctuations of R that are due to seasonal fluctuations of physical albedo (e.g. the melting of ice during summer) as well as those directly due to I. To separate the two effects we calculate the temporal average value of α, $\mathcal{T}(\alpha) = \mathcal{T}(R)/\mathcal{T}(I)$, to then decompose R as $R_{\text{solar}} = \mathcal{T}(\alpha)I$ and $R_{\text{internal}} = R - R_{\text{solar}}$ (this is done for each hemisphere, after hemispheric averaging). For both hemispheres $\mathcal{T}(\alpha) \approx 0.291$. In essence, R_{solar} is the R we would observe if we replaced Earth with a completely static, time-averaged version of itself.

Even in this decomposition, which disentangles the internal and solar fluctuations (Fig. 4), the insolation accounts for most of the variability of R. Specifically for the NH, 84% of the variance of R is attributed to R_{solar}, only 1% to R_{internal} and 13% to their co-variability. For the SH the numbers are 68%, 3% and 28%. A lack of power in Fourier components other than those corresponding to the seasonal cycle (1 and 0.5 years, Fig. 4b) in R_{internal} is consistent with our earlier analysis, which failed to distinguish R' from noise.

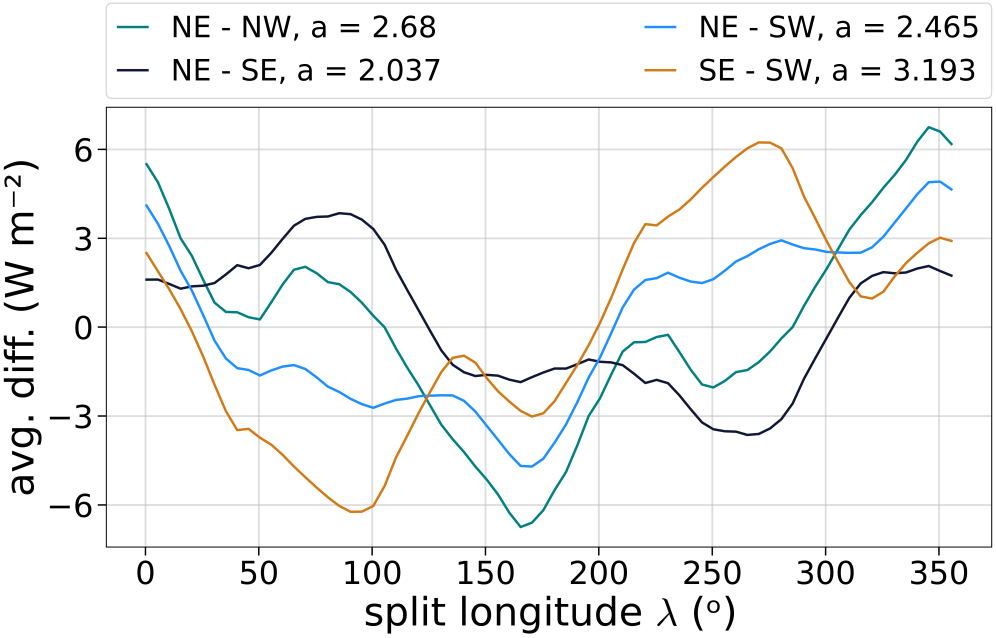

Figure 5. R is split into four quadrants at given longitude λ. The difference of the temporal & spatial averages between all four combinations of quadrants is plotted as a function of λ. a is the mean of the absolute value of each curve.

2.4 Secular trends and hemispheric co-variances

The lack of signal in R' makes the magnitude of its secular trend surprising. From the best-fit of the residuals we estimate its magnitude to be $0.7\,\mathrm{W\,m^{-2}}$ per decade. Part of this can be explained by a trend $\mathcal{G}(I)$, which is thought to arise from the the 11-year solar cycle and the shortness of the CERES record, which began near a solar maximum and ends near a solar minimum. However the trend in $\mathcal{G}(I)$ is only $0.36\,\mathrm{mW\,m^{-2}}$ per decade, hence $\alpha\mathcal{G}(I)$ can only explain about 15 % of the observed trend in $\mathcal{G}(R')$.

To develop a sense of the magnitude of the trend in $\mathcal{G}(R')$, we compare that part of its value not explained by the trend in $\mathcal{G}(I)$ to roughly 0.2 K per decade rise in globally averaged surface temperatures since 2000. If the former were attributed to the latter it would imply a positive albedo feedback greater than $0.7\times(1-0.15)/0.2 = 2.4\,\mathrm{W\,m^{-2}\,K^{-1}}$. This is a factor of three or more larger than assessed values (Sherwood et al. (2020) report a central estimate of $0.75\,\mathrm{W\,m^{-2}\,K^{-1}}$), which is to say it is a large number. The trend, first identified and analyzed by Loeb et al. (2020), was attributed to changes in north-eastern Pacific stratocumulus forced by decadal variations in sea-surface temperatures, in a way that models appear to largely capture. What hasn't been previously noted, and what we find difficult to explain given the lack of dynamics in R', is why a trend in $\mathcal{N}(R')$ attributed to changes in stratocumulus in the north-east pacific, is so well mirrored by much less spatially coherent (Loeb et al., 2020), but equal, changes in $\mathcal{S}(R')$. Were a substantial (more than a third) part of the observed trend attributable to global warming, it would have dramatic consequences. Put more broadly, if usefully quantifying the pace of global warming requires an ability to understand and quantify cloud responses to warming on the order of $0.2\,\mathrm{W\,m^{-2}\,K^{-1}}$, then surely more effort, building on prescient work by Loeb et al. (2020), to understand tenfold larger trends, and their symmetry, is warranted.

Despite our inability to distinguish detrended values of R' from noise, the similarity of the trends in $\mathcal{N}(R')$ and $\mathcal{S}(R')$ makes a case for hemispheric communication. This case is bolstered by an analysis of quadrants (semi-hemi-spheres). First, we perform a simple analysis that shows that there is little evidence for a process operating on sub-hemispheric scales that enforces a specific albedo value, which by chance is the same for both hemispheres. For this we split each hemisphere into two halves (quadrants) separated by the great circle aligned with the longitude λ. We then calculate the average difference of R between all six combinations of quadrants as a function of λ, (we present only four, because due to the process scanning all $\lambda \in [0, 360)$, we get NE-SW $\equiv$ NW-SE and NE-SE $\equiv$ NW-SW). Differences between arbitrary quadrants are, on average, much (by more than an order of magnitude) larger than hemispheric differences as we show in Fig. 5. However, differences between quadrants taken from different hemispheres are robustly smaller than those taken from the same hemisphere. Albeit far from a rigorous proof, this is in line with what one would expect if there were some active method of hemispheric albedo compensation.

3 Cloudiness and albedo

In this section we quantify the contribution of cloudiness to α to investigate how cloud asymmetries compensate hemispheric asymmetries in α_K, the cloud-free albedo.

3.1 Defining cloudiness, C

We begin by creating a "cloudiness" field C that represents physical cloud albedo by combining two independent definitions of cloud albedo. These two definitions qualitatively agree with each other, and give us the confidence that our results do not depend (qualitatively) on the exact definition of cloudiness. Combining them allows us to take advantage of their differing properties: one is energetically consistent with I and R, the other can exist for $I = 0$.

The first definition for cloudiness is the *cloud contribution to atmosphere albedo*. Donohoe and Battisti (2011) provide equations that can decompose the TOA albedo into an additive contribution from the atmosphere and the surface, based on the radiative fluxes at the TOA and surface and assuming that the atmosphere can be approximated as a single, uniform layer described by a given albedo and transparency, having the same scattering properties regardless if radiation comes from upwards or downwards. Loeb et al. (2019) extended the model to decompose time anomalies. Here we use the same model to decompose the planetary albedo into a surface (SFC) and atmoshere (ATM) contributions $\alpha = \alpha^{\mathrm{ATM}} + \alpha^{\mathrm{SFC}}$ and for clear-sky $\alpha_K = \alpha_K^{\mathrm{ATM}} + \alpha_K^{\mathrm{SFC}}$ as described in §Appendix A. These quantities allow us to define

$$C_\alpha = \alpha^{\mathrm{CLD}} = \alpha^{\mathrm{ATM}} - \alpha_K^{\mathrm{ATM}}. \tag{3}$$

An advantage of C_α, as compared to using the "cloud radiative effect" to define the cloudiness (as $(R-K)/I$), is that it does not conflate cloud with surface variability. Notice that C_α is effective and not physical albedo and is valid only for $I \neq 0$.

The second definition comes from a *cloud albedo parameterization* defined as

$$C_\tau = f \frac{\sqrt{3}(1-g)\tau}{2 + \sqrt{3}(1-g)\tau} \tag{4}$$

with f the cloud area fraction, τ the cloud optical depth, and g the asymmetry factor from the cloud particle phase function. Eq. (4) is the same as eq. (19) of Lacis and Hansen (1974), but multiplied with f. CERES (MODIS) provides f, and τ, but we have to estimate g (see below). The field τ has missing values, at the high-latitudes of the winter hemisphere. In Appendix A we describe a regularization process to fill these values.

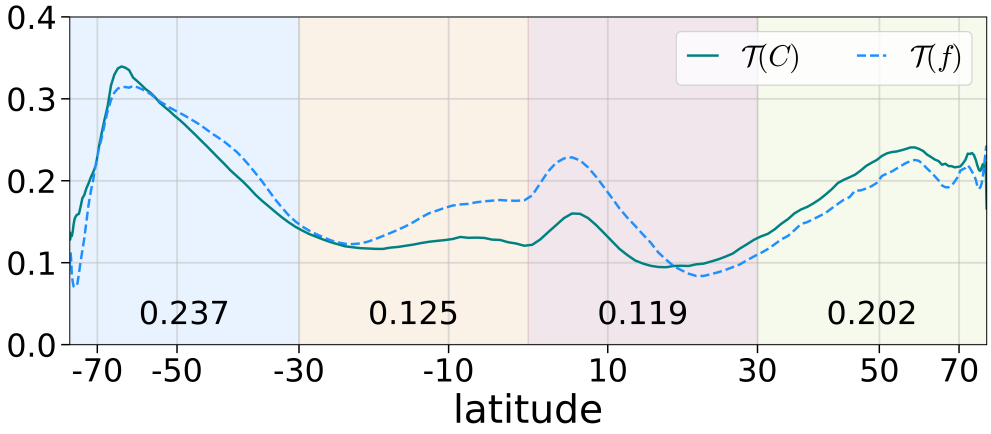

Figure 6. Temporally (and zonally) averaged cloudiness $\mathcal{T}(\mathcal{Z}(C))$ and cloud area fraction f (normalized for same mean and std. as C). We also display $\mathcal{C}$ averaged over four equal-area latitude zones (colored areas).

Using constant $g = 0.9$ for all grid points already gives very good qualitative agreement between C_α, C_τ in both temporally-averaged maps but also in spatially-averaged time-series.

Choosing g so that $\mathcal{T}(C_\tau - C_\alpha) = 0$ results in a physical cloud albedo, C_τ, that is energetically consistent with the time-averaged effective cloud albedo contribution, C_α, everywhere, but at the expense of g varying spatially. Because the spatial variations are small and within a physical range (see Appendix A), we adopt this approach, and denote the resultant cloud field by C. The reason for combining both definitions, by creating a spatially varying g, is that it allows us to define an energetically consistent cloud field that is also defined when $I = 0$. In addition, by testing that our results are qualitatively similar for two independent definitions of cloud albedo gives confidence in their robustness. For reference, temporally averaged maps of C, f, τ, g are shown in Fig. A2.

3.2 Mean cloudiness

Temporally and zonally averaged distributions of C are presented in Fig. 6 and compared to the cloud fraction f (normalized so that it has same mean and standard deviation as C). This shows that simply using f to represent cloudiness overestimates the impact of clouds in the deep tropics (equatorward of about 20°). As measured by C, the tropics are substantially less cloudy than the extra-tropics. Additionally, despite large latitudinal variations in cloud regimes – with the intra-tropical convergence zone being mostly north of the equator – C varies little (by less than 15 %) with latitude within the tropics.

Hemispherically, $\mathcal{T}(\mathcal{N}(C)) \approx 0.16$, compared to $\mathcal{T}(\mathcal{S}(C)) \approx 0.18$. Hence the southern hemisphere is cloudier by ≈ 0.02 – about 12% of the global average value. This asymmetry in C is (see Fig. 6) largely a result of the SH extra-tropics being much cloudier than the NH extra-tropics. This asymmetry is already evident in early cloud climatologies (Arrhenius, 1896; Brooks, 1927), its quantification here shows its importance for compensating the hemispheric asymmetry of the surface albedo.

In principle, asymmetries in C need not imply asymmetries in the effective albedo (and hence R). For example, were the asymmetries carried by nocturnal cloudiness they would have no effect on R. Qualitatively however, the asymmetry in cloudiness is suf-

ficient to establish the hemispheric albedo symmetry (i.e. on first order the spatio-temporal characteristics of C don't matter). Because the hemispheric difference of C represents an effective albedo value, and because the clear-sky albedo difference is $\delta\bar{\alpha}_K = \mathcal{T}(\mathcal{N}(K))/\mathcal{T}(\mathcal{N}(I)) - \mathcal{T}(\mathcal{S}(K))/\mathcal{T}(\mathcal{S}(I)) \approx 0.02$, then the hemispheric difference of C is sufficient to counter that of K. Using the model of Donohoe and Battisti (2011), increasing the atmospheric contribution to TOA albedo by 0.02 units gives a total TOA albedo increase of ≈ 0.02 for a wide range of choices of surface albedo, atmosphere albedo and atmosphere transmittance. This does not prove that hemispheric differences in the mean cloudiness compensate asymmetries in K, but suggests that it could.

3.3 Correlation with the solar cycle

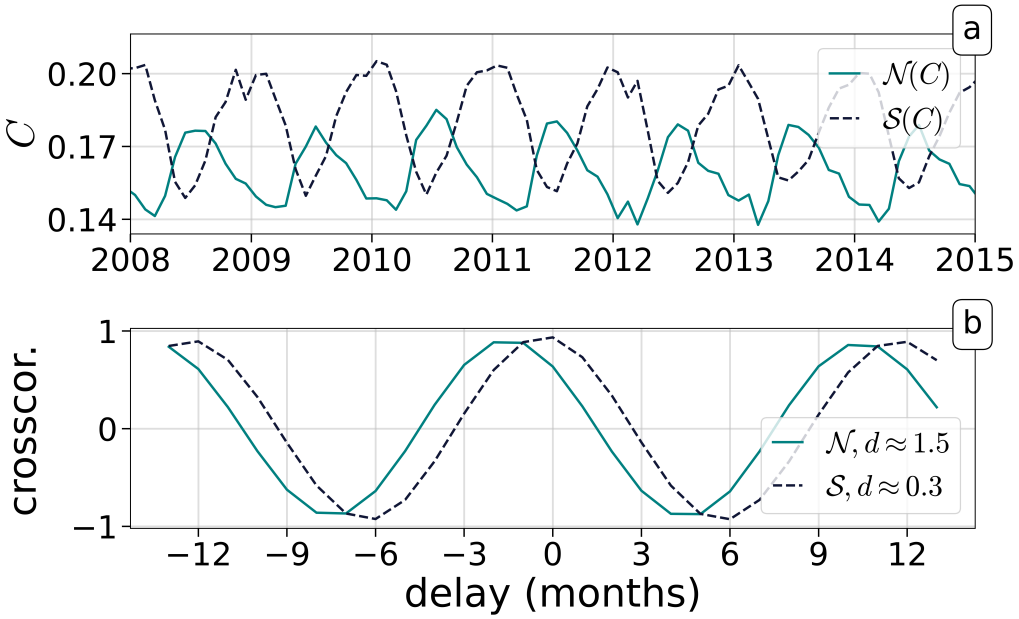

Figure 7. a: Cloudiness time-series, see eq. (4). A smaller time window is plotted for visual clarity. b: Temporal cross-correlation of C with I (for northern and southern hemispheric averages). The phase of the cross-correlations d is obtained by fitting $\cos(\text{delay} + d)$ to the curves.

In addition to hemispheric differences in the temporal and spatially averaged cloudiness, another candidate for compensating asymmetries in K is asymmetries in the covariability between I and C. In Fig. 7a we show hemispherically-averaged time-series of C and in Fig. 7b the cross-correlation function of the hemispherically averaged time-series of cloudiness C and insolation I. C is strongly linearly correlated with I (maximum cross-correlation values are ≈ 1), which is not surprising since cloudiness has a strong annual cycle. What we did not expect is the different delays d in the maximum of the cross-correlation(which is the phase shift between C and I) between the two hemispheres.

For the SH C has its maximum approximately at the time of maximum insolation as $d \approx 0.3$ months is small. In the NH, $d \approx 1.5$ months is larger, and appears to mostly be attributable to clouds in the NH extra tropics (not shown), for reasons that remain unclear. The larger lag of cloudiness in the NH contributes a small but measurable contribution to the compensation of the clear-sky asymmetry. Shifting the cloudiness time-series by 1.2 months (the difference of the delays between NH and SH), increases the cloud reflection by $\approx 0.28\,\mathrm{W\,m^{-2}}$ – or about 10 % of what is required to balance the asymmetry in α_K.

3.4 Cloudiness over different surface types

Having established that extra-tropical asymmetries in C largely compensate for hemispheric asymmetries in α_K, here we ask whether these are predominantly associated with clouds over a particular type of surface. For instance, is the NH extra-tropics less cloudy by virtue NH land masses being less cloudy? We investigate this possibility by defining different surface types: O denotes the ice-free ocean area fraction, E the ice & snow coverage and $L = 1-O-E$ the ice-free land fraction. All three of these are spatiotemporal fields and O, E are accessible from CERES auxiliary datasets. To estimate cloudiness over the three different surface types here we use each one of O, E, L as statistical weights. For each point in time, and for each hemisphere, we perform a weighted spatial average (in addition to the standard weighting by area) of the field C with weight O, E or L. This gives us the average value of C over a specific surface type as a time-series. We then perform a temporal average $\mathcal{T}$ and present the results in Fig. 8. Differences between the two hemispheres can be directly compared with the average hemispheric difference of C of ≈ 0.02. Taking the co-variability of clouds and ice into account mostly impacts the results for C over ice, which makes sense given that E varies much more than L, O.

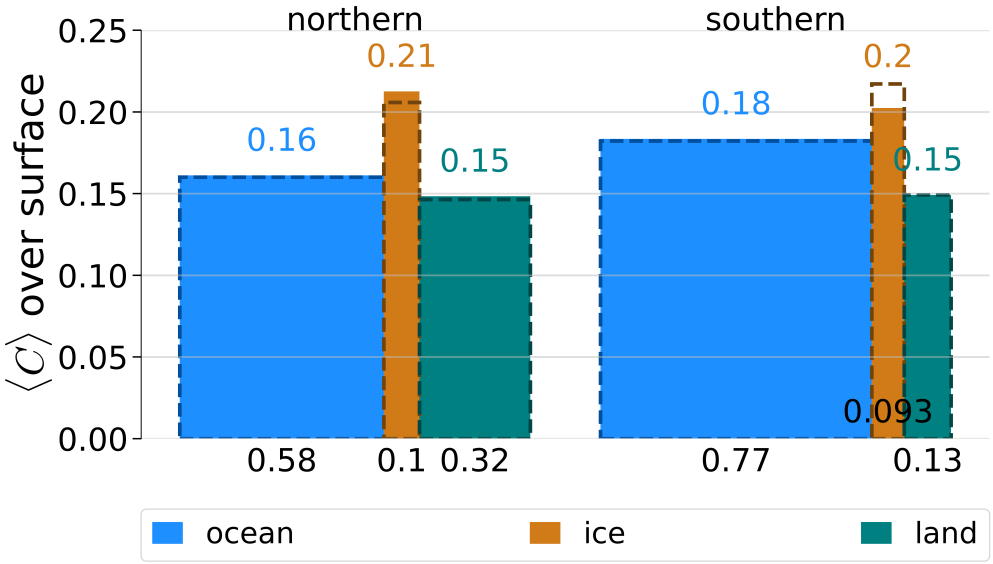

Figure 8. Average cloudiness C (height of the bars, also colored numbers) over different surface types. The width of the bars (also black numbers) is the surface fraction of that type. The dashed version of the bars is the numeric result of not taking co-variability of clouds and ice into account.

A trivial explanation for a compensating cloud contribution to the hemispheric clear-sky, α_K, asymmetry would be that land is less cloudy than ocean, in a way that directly compensates for its reduced surface albedo relative to the ocean. Neglecting contributions from ice-covered surfaces, and given that the land fraction is $\approx 19\,\%$ more in the NH than in the SH (Fig. 8), a 0.02 difference in C would require an $C_O - C_L \approx 0.11$ Fig. 8 shows that differences between C_L and C_O are much smaller than this. Instead the main difference between the cloudiness in the NH and that in the SH appears to be that the extra-tropical oceans of the SH are much cloudier than their counterpart in the NH (as seen by combining the information in Figs. 6 and 8).

4 Conclusions

We use twenty years of CERES data to study the global properties of Earth's planetary albedo, α. This quantity, which we define as the ratio of the reflected solar irradiance, R, to the insolation, I, is estimated as 0.291, consistent with many earlier estimates using the same, or similar data. The hemispheric albedo asymmetry, defined as the difference between the temporal and hemispheric averages of R is estimated as $0.10(28)\,\mathrm{W\,m^{-2}}$. The uncertainty (two sigma) is estimated using surrogate time-series and indicates that the measured asymmetry is indistinguishable from zero. In contrast, the hemispheric albedo asymmetry in the absence of clouds is a substantial fraction ($6\,\mathrm{W\,m^{-2}}$ or 11 %) of its global mean.

By constructing a quantitative measure of physical cloud albedo C we can decouple seasonality in clouds from those in insolation, and better quantify how cloud asymmetries compensate asymmetries in the cloud-free albedo to establish Earth's hemispheric albedo symmetry. This analysis identifies the global tropics (equatorward of 30°) as surprisingly transparent, with a zonally and temporally averaged value of C of 0.12 varying little with latitude. The extra-tropics are nearly twice as cloudy, the southern hemisphere (0.24) substantially more so than the northern hemisphere (0.20). Differences between cloudiness in the northern and southern hemispheres are primarily found over the ocean. Whereas land is less cloudy than the ocean (0.15 versus 0.17), the differences are insufficient to compensate for differences in land versus ocean clear-sky reflectances. Cloudiness in the northern hemisphere lags the annual cycle of insolation substantially more than in the southern hemisphere (1.5 months versus 0.3 months), which reduces the NH albedo. The effect is small ($0.28\,\mathrm{W\,m^{-2}}$) compared to surface albedo asymmetries. Where past work (Voigt et al., 2014) has investigated the role of shifts in tropical clouds as a means of symmetrizing the hemispheric albedo, the CERES data indicates that the asymmetry between the southern and northern hemispheric extra-tropical storm tracks is responsible for compensating hemispheric asymmetries in the cloud-free planetary albedo. The broad dynamical similarity between extra-tropical storms in the two hemispheres (Kodama et al., 2019) makes this difference in cloudiness unexpected. If anything, microphysical arguments would lead one to expect more ready rain initiation and less cloudiness in the southern hemisphere storms.

Analysis of the reflected flux, R, shows that almost all (97 % to 99 %, southern (SH) and northern (NH) respectively) of its variability can be explained by a seasonal cycle consisting of an annual and semi-annual harmonic. This seasonal cycle is mostly (68 % to 84 % SH/NH) attributable to the seasonal variations in insolation. The rest comes from seasonal variations in cloudiness. Extra-seasonal variations, defined as the residual R', between R and its seasonal projection, are small ($\sigma_{R'} = 1.1\,\mathrm{W\,m^{-2}}$). Using a variety of methods from time-series analysis we are unable to distinguish the hemispheric residuals from noise, implying that they evolve independently of one another.

That the asymmetry in cloudiness counter-balancing the clear-sky albedo asymmetry is confined to clouds over the extra-tropical ocean would seems to argue against a hemispheric communication mechanism. At least were such a mechanism present we would have expected it to be associated with shifts in tropical rain bands, which modelling studies show are more closely associated with heat transport between the hemispheres (Kang et al., 2008). Further evidence against a dynamic mechanism that acts to symmetrise the hemispheric albedo is that there is so little signal of extra-seasonal variability in cloudiness, and that what signal there is, is indistinguishable from noise.

Given the lack of coherence, or correlated dynamics in the extra-seasonal component of R made the presence of a significant downward trend ($-0.7\,\mathrm{W\,m^{-2}}$ per decade) over the recorded period surprising. All the more surprising is that this trend, which previous literature has identified with a coherent mode of variability in north-east Pacific stratocumulus (Loeb et al., 2020), is almost identical in both hemispheres. This would

seem to argue for a dynamic mechanism which acts to maintain hemispheric albedo symmetry. An additional indicator of a possible mechanisms comes from an analysis of the albedo of semi-hemispheres. It shows that the symmetry between semi-spheres selected from different hemispheres is substantially greater than from semi-spheres within selected from the same hemisphere.

If the observed trend in R were attributable to the changes in observed surface temperatures, it would correspond to an exceptionally strong short-wave cloud feedback (greater than $2.4\,\mathrm{W\,m^{-2}\,K^{-1}}$) – enough to portend a run-away greenhouse effect. While we are skeptical of this interpretation, the magnitude of the signal, and its coincidence with a broader and unexplained pattern of cloudiness to be larger in the colder hemisphere, merits attention.

Acknowledgments
We acknowledge Ulrich Parlitz and Hauke Schmidt for fruitful scientific discussions regarding this work.

Data used and code base: Analysis is based on the monthly averaged CERES data. We use the Energy Balanced and Filled (EBAF) Ed. 4.1 (Loeb et al., 2018; Kato et al., 2018), data set. For cloud properties we use the SYN1deg data (Doelling et al., 2013; Rutan et al., 2015). We also use the auxiliary data of SYN1deg to get ice-free ocean and ice & snow area fractions. All data have spatial resolution of $1^\circ\times1^\circ$ and span from March 2000 to April 2020, totalling 242 months. All of these datasets are publicly available.

This work is also available as a fully reproducible code base `https://github.com/Datseris/EarthAlbedoSymmetry`. The absolute exact data used in this paper are archived in the same repository.

Appendix A Observational data processing for cloudiness

To derive the atmospheric and surface contributions to the albedo α we re-write the model of Donohoe and Battisti (2011) to obtain

$$\alpha^{\mathrm{ATM}} = \frac{(\alpha - a_s t^2)}{1-(a_s t)^2} \tag{A1}$$

$$\alpha^{\mathrm{SFC}} = \frac{a_s t^2 (1-\alpha^{\mathrm{TOA}} a_s)^2}{1-\alpha^{\mathrm{TOA}} a_s} \tag{A2}$$

with $\alpha = F^{\mathrm{TOA}}_{\uparrow}/F^{\mathrm{TOA}}_{\downarrow} \equiv R/I$ the planetary albedo, $t = F^{\mathrm{SFC}}_{\downarrow}/F^{\mathrm{TOA}}_{\downarrow}$ the planetary transmittance and $a_s = F^{\mathrm{SFC}}_{\uparrow}/F^{\mathrm{SFC}}_{\downarrow}$ the surface albedo which in general is different than the surface *contribution* to the planetary albedo due to further reflections between surface and atmosphere. F simply stands for shortwave radiation, and all necessary instances of F are provided in the same CERES dataset used throughout. Note that Stephens et al. (2015) adopted a similar approach, but arrived at slightly different expressions, which appear to be incorrect, or incorrectly typeset.

The optical depth field τ provided by CERES has missing values in a large portion of its time-series for spatial points near the poles. These missing values make hemispheric averages impossible and thus need to be "fixed". Here, we used a simple sinusoidal continuation, shown in Fig. A1. Using the same method as in §22.1, we fit sinusoidals of frequencies 1/year and 2/year to the available (i.e. non-missing) data. The value of the sinusoidal fit is used to fill in only the entries of τ that are missing. Furthermore, Fig. A2 shows temporally averaged maps of C, f, τ, g.

Different satellites and observational data products can have significant differences in both how they define and measure cloud area fraction f and optical depth τ, this will

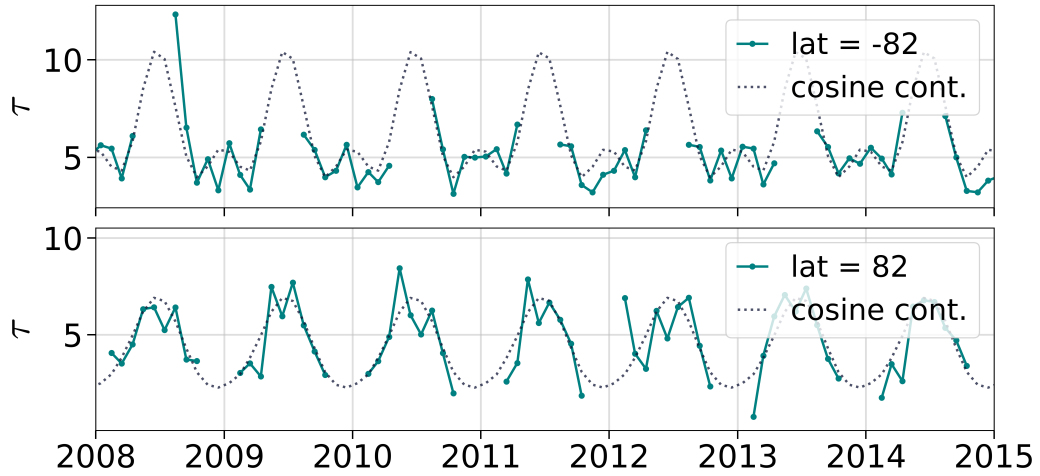

Figure A1. Continuation of the optical depth time-series τ.

cause differences in the diagnosed values of g chosen to maintain consistency between C_α and C.

References

Arrhenius, S. (1896, apr). On the influence of carbonic acid in the air upon the temperature of the ground. *The London, Edinburgh, and Dublin Philosophical Magazine and Journal of Science*, *41*(251), 237–276. Retrieved from `https://www.tandfonline.com/doi/full/10.1080/14786449608620846` doi: 10.1080/14786449608620846

Bagge Carlson, F., Robertsson, A., & Johansson, R. (2017, 07). Linear parameter-varying spectral decomposition. In *American control conference (acc), 2017* (pp. 146–151). Institute of Electrical and Electronics Engineers Inc. Retrieved from `https://lup.lub.lu.se/search/ws/files/20192000/LPVspectralestPaper.pdf` doi: 10.23919/ACC.2017.7962945

Bender, F. A., Engström, A., Wood, R., & Charlson, R. J. (2017). Evaluation of hemispheric asymmetries in marine cloud radiative properties. *Journal of Climate*, *30*(11), 4131–4147. doi: 10.1175/JCLI-D-16-0263.1

Betts, R. A. (2000, November). Offset of the potential carbon sink from boreal forestation by decreases in surface albedo. *Nature*, *408*(6809), 187–190. Retrieved from `https://doi.org/10.1038/35041545` doi: 10.1038/35041545

Brockwell, P. J., & Davis, R. A. (1996). *Introduction to time series and forecasting*. Springer New York. Retrieved from `https://doi.org/10.1007/978-1-4757-2526-1` doi: 10.1007/978-1-4757-2526-1

Brooks, C. (1927). The mean cloudiness over the Earth. *Mem. Roy. Meteorol. Soc.*, *1*, 127–138.

Budyko, M. I. (1969). The effect of solar radiation variations on the climate of the Earth. *Tellus*, *21*(5), 611–619. doi: 10.3402/tellusa.v21i5.10109

Chýlek, P., & Coakley, J. A. (1975, apr). Analytical Analysis of a Budyko-Type Climate Model. *Journal of the Atmospheric Sciences*, *32*(4), 675–679. Retrieved from `http://journals.ametsoc.org/doi/abs/10.1175/1520-0469{\%}281975{\%}29032{\%}3C0675{\%}3AAAOABT{\%}3E2.0.CO{\%}3B2` doi: 10.1175/1520-0469(1975)032⟨0675:AAOABT⟩2.0.CO;2

Cowan, N. B., & Agol, E. (2011, feb). THE STATISTICS OF ALBEDO AND

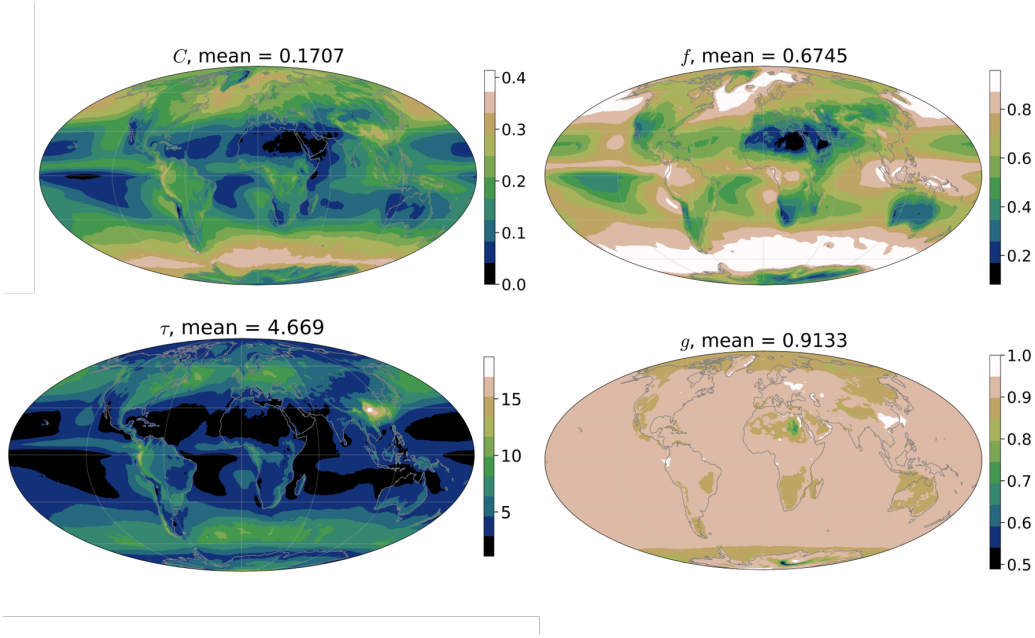

Figure A2. Temporally-averaged maps of fields used in the definition of effective cloud albedo, eq. (4). Shown also are the spatial means.

HEAT RECIRCULATION ON HOT EXOPLANETS. *The Astrophysical Journal*, *729*(1), 54. Retrieved from `https://doi.org/10.1088%2F0004-637x%2F729%2F1%2F54` doi: 10.1088/0004-637x/729/1/54

Doelling, D. R., Loeb, N. G., Keyes, D. F., Nordeen, M. L., Morstad, D., Nguyen, C., ... Sun, M. (2013, June). Geostationary enhanced temporal interpolation for CERES flux products. *Journal of Atmospheric and Oceanic Technology*, *30*(6), 1072–1090. Retrieved from `https://doi.org/10.1175/jtech-d-12-00136.1` doi: 10.1175/jtech-d-12-00136.1

Donohoe, A., & Battisti, D. S. (2011). Atmospheric and surface contributions to planetary albedo. *Journal of Climate*, *24*(16), 4402–4418. doi: 10.1175/2011JCLI3946.1

Haar, T. H. V., & Suomi, V. E. (1971, April). Measurements of the earth's radiation budget from satellites during a five-year period. part i: Extended time and space means. *Journal of the Atmospheric Sciences*, *28*(3), 305–314. Retrieved from `https://doi.org/10.1175/1520-0469(1971)028<0305:moterb>2.0.co;2` doi: 10.1175/1520-0469(1971)028⟨0305:moterb⟩2.0.co;2

Haywood, J. M., Jones, A., Dunstone, N., Milton, S., Vellinga, M., Bodas-Salcedo, A., ... Stephens, G. (2016, January). The impact of equilibrating hemispheric albedos on tropical performance in the HadGEM2-ES coupled climate model. *Geophysical Research Letters*, *43*(1), 395–403. Retrieved from `https://doi.org/10.1002/2015gl066903` doi: 10.1002/2015gl066903

Kang, S. M., Held, I. M., Frierson, D. M. W., & Zhao, M. (2008, July). The Response of the ITCZ to Extratropical Thermal Forcing: Idealized Slab-Ocean Experiments with a GCM. *Journal of Climate*, *21*(14), 3521–3532. doi: 10.1175/2007JCLI2146.1

Kato, S., Rose, F. G., Rutan, D. A., Thorsen, T. J., Loeb, N. G., Doelling, D. R., ... Ham, S.-H. (2018, May). Surface irradiances of edition 4.0 clouds and the earth's radiant energy system (CERES) energy balanced and filled (EBAF) data product. *Journal of Climate*, *31*(11), 4501–4527. Retrieved from

https://doi.org/10.1175/jcli-d-17-0523.1 doi: 10.1175/jcli-d-17-0523.1

Kodama, C., Stevens, B., Mauritsen, T., Seiki, T., & Satoh, M. (2019). A New Perspective for Future Precipitation Change from Intense Extratropical Cyclones. *Geophysical Research Letters*, *46*(21), 12435–12444. doi: 10.1029/2019GL084001

Kreidberg, L., Bean, J. L., Désert, J. M., Benneke, B., Deming, D., Stevenson, K. B., ... Homeier, D. (2014). Clouds in the atmosphere of the super-Earth exoplanet GJ 1214b. *Nature*, *505*(7481), 69–72. doi: 10.1038/nature12888

Lacis, A. A., & Hansen, J. (1974, jan). A Parameterization for the Absorption of Solar Radiation in the Earth's Atmosphere. *Journal of the Atmospheric Sciences*, *31*(1), 118–133. Retrieved from http://journals.ametsoc.org/doi/abs/10.1175/1520-0469{\%}281974{\%}29031{\%}3C0118{\%}3AAPFTAO{\%}3E2.0.CO{\%}3B2 doi: 10.1175/1520-0469(1974)031⟨0118:APFTAO⟩2.0.CO;2

Lancaster, G., Iatsenko, D., Pidde, A., Ticcinelli, V., & Stefanovska, A. (2018). Surrogate data for hypothesis testing of physical systems. *Physics Reports*, *748*, 1–60. Retrieved from https://doi.org/10.1016/j.physrep.2018.06.001 doi: 10.1016/j.physrep.2018.06.001

Levinson, N. (1946, April). The wiener (root mean square) error criterion in filter design and prediction. *Journal of Mathematics and Physics*, *25*(1-4), 261–278. Retrieved from https://doi.org/10.1002/sapm1946251261 doi: 10.1002/sapm1946251261

Loeb, N. G., Doelling, D. R., Wang, H., Su, W., Nguyen, C., Corbett, J. G., ... Kato, S. (2018, January). Clouds and the earth's radiant energy system (CERES) energy balanced and filled (EBAF) top-of-atmosphere (TOA) edition-4.0 data product. *Journal of Climate*, *31*(2), 895–918. Retrieved from https://doi.org/10.1175/jcli-d-17-0208.1 doi: 10.1175/jcli-d-17-0208.1

Loeb, N. G., Wang, H., Allan, R., Andrews, T., Armour, K., Cole, J. N. S., ... Wyser, K. (2020). New Generation of Climate Models Track Recent Unprecedented Changes in Earth's Radiation Budget Observed by CERES. *Geophysical Research Letters*, *n/a*(n/a), e2019GL086705. Retrieved from https://doi.org/10.1029/2019GL086705 doi: 10.1029/2019GL086705

Loeb, N. G., Wang, H., Rose, F. G., Kato, S., Smith, W. L., & Sun-Mack, S. (2019). Decomposing shortwave top-of-atmosphere and surface radiative flux variations in terms of surface and atmospheric contributions. *Journal of Climate*, *32*(16), 5003–5019. doi: 10.1175/JCLI-D-18-0826.1

Mansfield, M., Kite, E. S., Hu, R., Koll, D. D. B., Malik, M., Bean, J. L., & Kempton, E. M.-R. (2019, dec). Identifying atmospheres on rocky exoplanets through inferred high albedo. *The Astrophysical Journal*, *886*(2), 141. Retrieved from https://doi.org/10.3847%2F1538-4357%2Fab4c90 doi: 10.3847/1538-4357/ab4c90

Nakamura, T., Small, M., & Hirata, Y. (2006, Aug). Testing for nonlinearity in irregular fluctuations with long-term trends. *Phys. Rev. E*, *74*, 026205. Retrieved from https://link.aps.org/doi/10.1103/PhysRevE.74.026205 doi: 10.1103/PhysRevE.74.026205

North, G. R. (1975). *Theory of Energy-Balance Climate Models* (Vol. 32) (No. 11). doi: 10.1175/1520-0469(1975)032⟨2033:TOEBCM⟩2.0.CO;2

Ramanathan, V. (1987). The role of earth radiation budget studies in climate and general circulation research. *Journal of Geophysical Research*, *92*(D4), 4075. doi: 10.1029/jd092id04p04075

Rutan, D. A., Kato, S., Doelling, D. R., Rose, F. G., Nguyen, L. T., Caldwell, T. E., & Loeb, N. G. (2015, June). CERES synoptic product: Methodology and validation of surface radiant flux. *Journal of Atmospheric and Oceanic Technology*, *32*(6), 1121–1143. Retrieved from https://doi.org/10.1175/jtech-d-14-00165.1 doi: 10.1175/jtech-d-14-00165.1

Scholz, F. W., & Stephens, M. A. (1987, September). K-sample anderson-darling

tests. *Journal of the American Statistical Association*, *82*(399), 918. Retrieved from https://doi.org/10.2307/2288805 doi: 10.2307/2288805

Sellers, W. D. (1969). *Global Climatic Model Based on the Energy Balance of the Earth- Atmosphere System* (Vol. 8) (No. 3).

Sherwood, S., Webb, M. J., Annan, J. D., Armour, K. C., Forster, P. M., Hargreaves, J. C., ... Zelinka, M. D. (2020). An assessment of Earth's climate sensitivity using multiple lines of evidence. *Reviews of Geophysics*. doi: 10.1029/2019RG000678

Shields, A. L., Meadows, V. S., Bitz, C. M., Pierrehumbert, R. T., Joshi, M. M., & Robinson, T. D. (2013, August). The effect of host star spectral energy distribution and ice-albedo feedback on the climate of extrasolar planets. *Astrobiology*, *13*(8), 715–739. Retrieved from https://doi.org/10.1089/ast.2012.0961 doi: 10.1089/ast.2012.0961

Small, M., Yu, D., & Harrison, R. G. (2001). Surrogate test for pseudoperiodic time series data. *Physical Review Letters*, *87*(18), 188101–1–188101–4. doi: 10.1103/PhysRevLett.87.188101

Stephens, G. L., Hakuba, M. Z., Hawcroft, M., Haywood, J. M., Behrangi, A., Kay, J. E., & Webster, P. J. (2016). The Curious Nature of the Hemispheric Symmetry of the Earth's Water and Energy Balances. *Current Climate Change Reports*, *2*(4), 135–147. Retrieved from http://dx.doi.org/10.1007/s40641-016-0043-9 doi: 10.1007/s40641-016-0043-9

Stephens, G. L., O'Brien, D., Webster, P. J., Pilewski, P., Kato, S., & Li, J.-l. (2015, mar). The albedo of Earth. *Reviews of Geophysics*, *53*(1), 141–163. Retrieved from http://doi.wiley.com/10.1002/2014RG000449 doi: 10.1002/2014RG000449

Stevens, B., & Schwartz, S. E. (2012). Observing and Modeling Earth's Energy Flows. *Surveys in Geophysics*, *33*(3-4), 779–816. doi: 10.1007/s10712-012-9184-0

Stone, P. H. (1978). Constraints on dynamical transports of energy on a spherical planet. *Dynamics of Atmospheres and Oceans*, *2*(2), 123–139. doi: 10.1016/0377-0265(78)90006-4

Theiler, J., Eubank, S., Longtin, A., Galdrikian, B., & Doyne Farmer, J. (1992). Testing for nonlinearity in time series: the method of surrogate data. *Physica D: Nonlinear Phenomena*, *58*(1-4), 77–94. doi: 10.1016/0167-2789(92)90102-S

Voigt, A., Stevens, B., Bader, J., & Mauritsen, T. (2013). The observed hemispheric symmetry in reflected shortwave irradiance. *Journal of Climate*, *26*(2), 468–477. doi: 10.1175/JCLI-D-12-00132.1

Voigt, A., Stevens, B., Bader, J., & Mauritsen, T. (2014). Compensation of hemispheric albedo asymmetries by shifts of the ITCZ and tropical clouds. *Journal of Climate*, *27*(3), 1029–1045. doi: 10.1175/JCLI-D-13-00205.1